ACS SENSORS

pubs.acs.org/acssensors

Article

SARS-CoV-2-Impedimetric Biosensor: Virus-Imprinted Chips for Early and Rapid Diagnosis

Heba A. Hussein, Ahmed Kandeil, Mokhtar Gomaa, Rasha Mohamed El Nashar, Ibrahim M. El-Sherbiny, and Rabeay Y. A. Hassan*

Cite This: https://doi.org/10.1021/acssensors.1c01614

Read Online

ACCESS | Metrics & More | Article Recommendations | Supporting Information

ABSTRACT: Due to the current global SARS-CoV-2 pandemic, rapid and accurate diagnostic tools are needed to prevent the spread of COVID-19 across the globe. An electrochemical sensing platform was constructed using CNTs/WO_3-screen printed electrodes for imprinting the complete virus particles (SARS-CoV-2 particles) within the polymeric matrix to create viral complementary binding sites. The sensor provided high selectivity toward the target virus over other tested human corona and influenza respiratory interference viruses. The sensitivity performance of the sensor chips was evaluated using different viral concentrations, while the limits of detection and quantification were 57 and 175 pg/mL, respectively. Reaching this satisfied low detection limit (almost 27-fold more sensitive than the RT-PCR), the sensor was applied in clinical specimens obtained from SARS-CoV-2 suspected cases. Thus, dealing directly with clinical samples on the chip could be provided as a portable device for instantaneous and simple point of care in hospitals, airports, and hotspots.

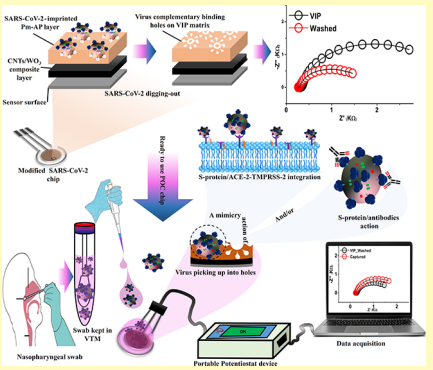

KEYWORDS: *COVID-19, SARS-CoV-2 biosensors, impedimetric biosensors, carbon nanotubes/tungsten oxide, point of care (POC), personal diagnostics*

The current pandemic of coronavirus-associated severe acute respiratory syndrome coronavirus 2 (SARS-CoV-2) is the third documented animal coronavirus transmitted to humans in the past two decades that has resulted in a global epidemic.[1] The virus is an isolated species of lineage B related to beta-coronaviruses, subgenus sarbecovirus, which is associated with an evolutionary history since the SARS-CoV outbreaks in 2002 till the emerging attack of SARS-CoV-2 in 2019.[2−4] Like other coronaviridae, SARS-CoV-2 is encoded of multiple structural and non-structural proteins in its 30 kb single-stranded positive-sense RNA.[5]

The cell entry is mediated by trimeric glycosylated spike proteins.[6] The cellular entry imposes the S-protein priming by transmembrane protease, serine 2, resulting in S-protein cleavage into S1 and S2 subunits. The S1 is responsible for receptor binding, while the S2 provides the fusion of viral and cellular membranes.[7,8]

Common virus diagnosis primarily relies on two laboratory axes: direct diagnosis with the molecular detection of the nucleic acids using reverse transcription-polymerase chain reaction (RT-PCR)[9] or indirect diagnosis using serological profiling against the viral infection (virus propagation). The former has many drawbacks including being time-consuming, reaching 6−7 h for specimen genomic extraction and amplification, requiring a well-equipped lab, and qualified expertise.[2] On the other hand, antibody response takes from several days to weeks to be developed in the patient serum post-infection.[10]

Recently, electrochemical biosensors have been deployed in viral infection detection techniques due to their robustness in test performance, immediate sample investigation in the presence of a minimum concentration of the analyte, and miniaturized devices.[11,12] For instance, a graphene-based field-effect transistor (FET) was developed for the rapid detection of SARS-CoV-2 particles in clinical specimens.[13] The graphene layer was coated with an anti-SARS-CoV-2 spike (S)-protein for the COVID-19 diagnostic test in clinical specimens. The detection limits of that sensor were 160 pfu/mL and 24,200 copies/mL in the SARS-CoV-2 culture medium and clinical samples, respectively.[14]

Furthermore, antisense oligonucleotide probes were used for gold nanoparticle coating to detect the virus RNA. Formerly, a selective colorimetric assay was developed after the agglomeration of thiolated-oligos-capped gold nanoparticles with the target SARS-CoV-2 genetic thread and the detection limit was 0.18 ng/μL SARS-CoV-2-RNA.[15] Later, gold nanoparticles

Received: July 29, 2021
Accepted: November 1, 2021

Scheme 1. Steps of SARS-CoV-2 VIP Sensor Fabrication, Including Surface Modification with CNTs/WO_3, Virus Imprinting, and Virus Particle Removal to Create a Template for the Specific Recognition of the SARS-CoV-2[a]

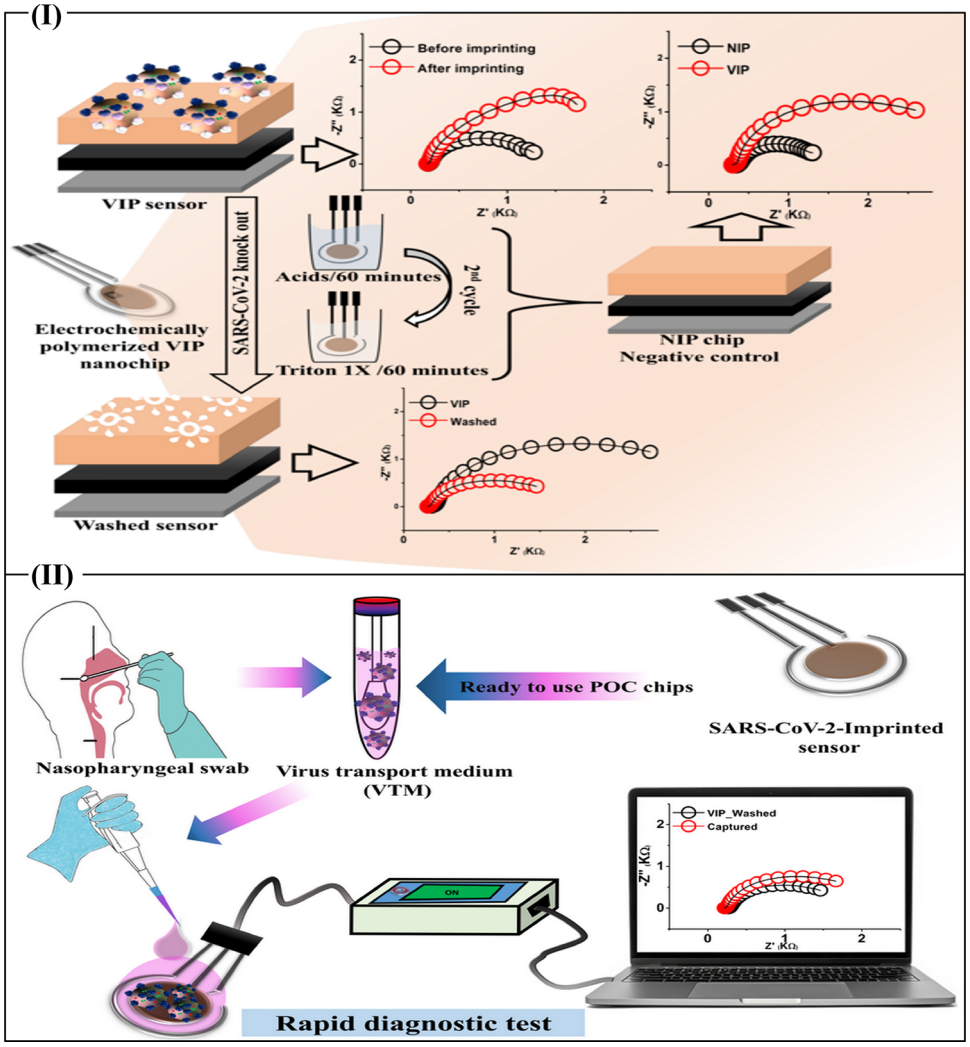

[a]Double-mediating FCN/DCIP solution free from the virus, and the non-imprinted electrode (NIP) was used as a control for each step of the sensor fabrication (I). Testing the designed VIP sensor for clinical sample analysis (II).

were capped with antisense oligonucleotide probes to target the SARS-CoV-2-N-protein. This platform was carried out by oligonucleotide probe immobilization on a paper-based electrochemical platform. The sensor detected the virus-N-protein in the virus culture and clinical samples within 5 min with a 6.9 copies/μL detection limit.[16] On the other hand, tailor-made plastic antibodies created by molecularly imprinted polymers (MIPs) were integrated into biosensing platforms.[17] Therefore, virus-imprinted sensors (VIP) were exploited for selective and rapid detection of animal and human viruses.[18] In this regard, an MIP-based electrochemical sensor was developed using poly-*m*-phenylenediamine on gold-based thin-film electrodes for the SARS-CoV-2-N-protein; the resulting limits of detection and quantification were 15 and 50 fM, respectively.[19]

Herein, a DCIP/FCN-mediated impedimetric virus sensor is designed for the rapid detection of the whole SARS-CoV-2 particles using a modified screen-printed electrode with CNTs/WO_3. The sensor provides an on-site investigation of whole virus particles in clinical specimens directly without sample preparation, as illustrated in Scheme 1.

MATERIALS AND METHODS

SARS-CoV-2 Propagation and Purification. An identified (hCoV-19/Egypt/NRC-03/2020 SARS-CoV-2 strain (GISAID accession number: EPI-ISL-430820)) oropharyngeal swab specimen was obtained from a 34 year old woman from El-Minya governorate, Egypt.[20] The specimen was propagated in a Vero-E6 cell line for two successive passages for 3 days of incubation at 37 °C in a 5−6% CO_2 incubator. The virus suspension was clarified twice by centrifugation at 4500 rpm for 30 min at 4 °C. With 20% sucrose, the suspension was ultracentrifuged for 1 h at 4 °C at 50,000*g*. The total antigenic payload was measured using a NanoDrop 2000c. The concentrated antigen was stored at −80 °C until further use.

Sensor Surface Modification and SARS-CoV-2 Imprinting. Electrochemical measurements were carried out using a computer-controlled Palmsens-4 potentiostat/galvanostat/impedance analyzer. As a sensor platform, screen-printed carbon electrodes (SPEs) were used. The working area of the SPE was modified with nanomaterials including AuNPs, MWCNTs, and fullerene and metal oxides such as MnO_2 and WO_3. In addition, composites of these materials were prepared and their electrochemical characteristics were identified. In this regard, cyclic voltammetry (CV) was carried out at a scan rate of 50 mV/s and the applied potential range from −0.4 to 1.0 V vs Ag/AgCl. Electrochemical impedance spectroscopy (EIS) was conducted

https://doi.org/10.1021/acssensors.1c01614
ACS Sens. XXXX, XXX, XXX−XXX

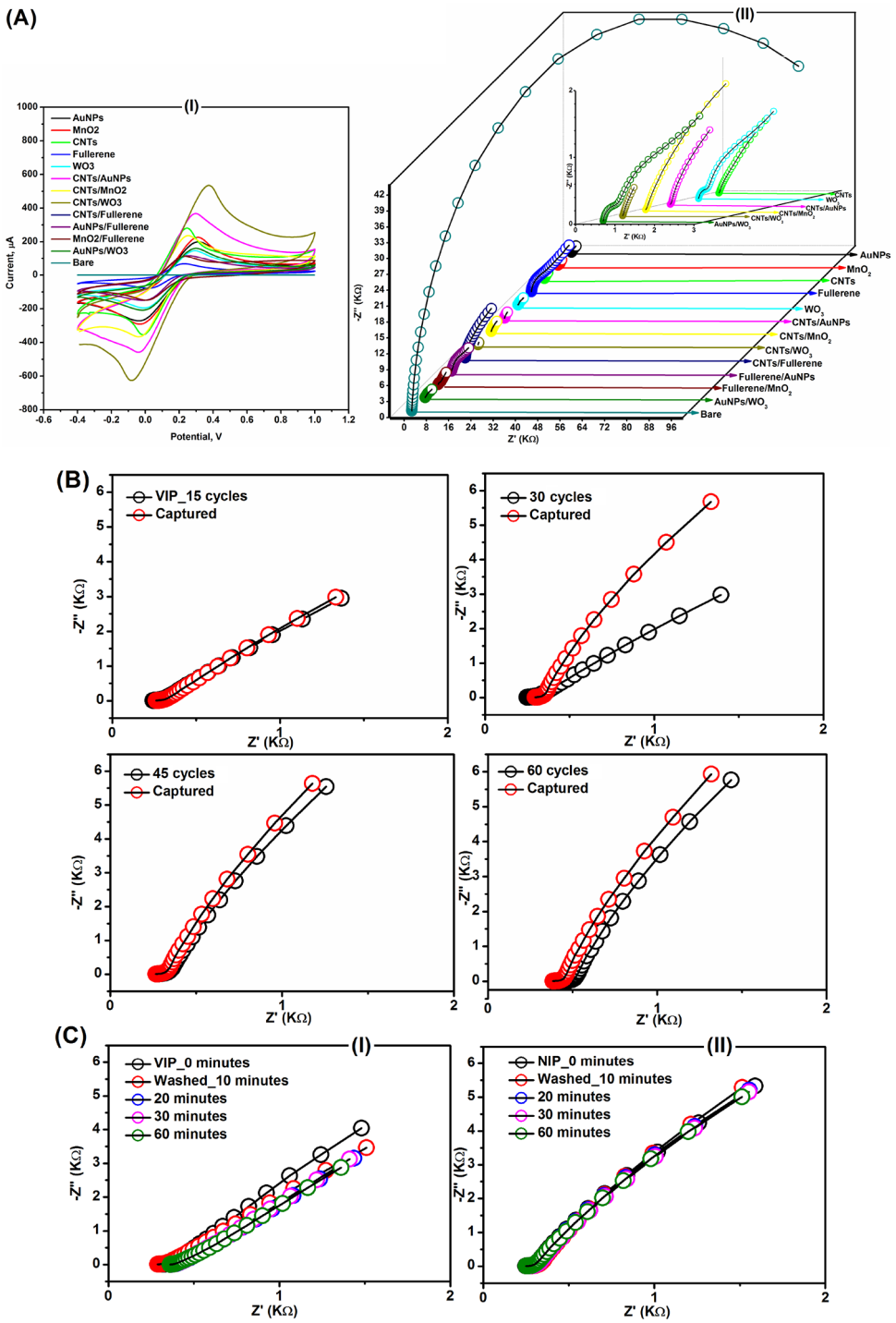

Figure 1. (A) Electrochemical characterization of the modified sensor surface in 1 mM FCN with different nanomaterials using CV at a potential range from −0.4 to 1 V and a scan rate of 50 mV/s (I) and EIS at an AC potential of 0.005 V and the applied frequency sweeps extended from 1 MHz to 0.1 Hz (II). The CNTs/WO_3-modified electrodes provided the best electrochemical responses. (B) SARS-CoV-2 imprinting using different numbers of voltammetric cycles: EIS signals showed that 30 voltammetric cycles were efficient. The remarkable signals were obtained from the washed and captured ones. (C) Washing time effect on the virus disruption: responses of the VIP matrix (I) where the virus disruption is measurable coinciding with the incubation time (10−60 min) compared to the responses of the polymeric matrix alone where no virus is imprinted (NIP) (II).

at an AC potential of 5 mV, and the applied frequency sweeps were extended from 10,000 to 0.1 Hz. Potassium ferrocyanide(III) (FCN, Merck, USA) was used as the standard redox probe for the CV and EIS characterizations. From the nanomaterial screening step, the CNTs/WO_3 nanocomposite at a ratio of 2:1 (v/v) was selected and employed as the sensor platform for the electrochemical imprinting of SARS-CoV-2 particles. Thus, a suspension of the virus particles (2.16 µg/mL) in an aqueous solution of a monomer (3-aminophenol, m-AP, 98%, Sigma-Aldrich, 0.1 M in PBS, pH = 7.4) was electropolymerized. The process was carried out at a potential range from −0.4 to 1.4 V for 30 successive voltammetric cycles at a 50 mV/s scan rate. The process was conducted in the absence of SARS-CoV-2 as a negative control.

https://doi.org/10.1021/acssensors.1c01614
ACS Sens. XXXX, XXX, XXX−XXX

SARS-CoV-2 Removal from the Layered VIP Matrix. The template for the specific recognition of the SARS-CoV-2 was created onto the VIP matrix via soaking the imprinted surfaces in acidic solution (4% citric + 6% acetic acid, pH of 2.4) for 60 min at room temperature. Subsequently, the VIP sensor was subjected to another washing cycle in 1× Triton solution for 30 min at room temperature. In parallel, 1% sodium hypochlorite and 70% ethanol solutions were used in the virus dig out from the VIP chips. The effect of the washing solutions on the virus particles was inspected using TEM after incubation with the washing solutions. The virus suspension was loaded on carbon/copper TEM grids for about 10 min, and then the loaded grids were fixed in 2.5% glutaraldehyde for 2 h and subsequently stained with 3% phosphotungstic acid for 10 min.

Sensor Performance Test. EIS measurements (non-mediated or mediated with 100 μM 2,6-dichlorophenolindophenol (DCIP), 0.3 mM FCN, or a mixture of both mediators) were conducted to evaluate the sensing efficacy of the complementary binding sites created on the VIP matrix. Nine different virus concentrations (7, 50, 90, 130, 180, 210, 290, and 320 pg/mL) were used to test the sensor performance. EIS signals were recorded in FCN/DCIP before and after the in situ capturing of virus particles at 1 V potential (DC), and the applied frequency sweeps were extended from 10,000 to 0.1 Hz.

Impedimetric Circuit Model. An equivalent electrical circuit was modeled including the solution resistance (Rs), the capacitance of the electrode surface outer layer (C1), electron transfer resistance (R2) of the CNTs/WO_3 layer, constant phase elements of the inner layer of the electrode (CPE1), the double-layer capacitance of the deposited polymeric matrix (poly(*m*-aminophenol) (PmAP)) on the electrode (C2), the resistance of the captured virus particles (R3), and, eventually, the Warburg impedance (W1) displaying the diffusion of the FCN/DCIP mediators. Thus, from the designed Randles cell circuit, the best match between the obtained electrochemical impedance spectra and the designed equivalent circuit models was used for statistical analysis as well as the sensor's performance and application in clinical samples.

Selectivity Testing. Several respiratory interferent viruses were tested using the designed sensor. In this regard, Influenza A viruses (H_1N_1, H_5N_1, and H_3N_2), Influenza B, human coronaviruses (hCoVs)-OC43, NL63, and 229E, and the Middle East respiratory syndrome coronavirus (MERS-CoV) were exposed to the sensors, and their electrochemical impedimetric responses were measured. Each interfering virus was tested solely or in a mixture including and excluding the target virus. To avoid the non-specific response, the sensor chips were rinsed three times with PBS to flush away the non-captured particles. Eventually, impedimetric analysis was performed in a FCN/DCIP double-mediated system at 1.0 V potential (DC) and the applied frequency sweeps were extended from 10,000 to 0.1 Hz.

Application of the SARS-CoV-2 Sensor in Clinical Samples. As the oropharyngeal and/or nasopharyngeal swabs are the commonly preferable samples for SARS-CoV-2 diagnosis, 5 μL of each of the clinical specimens was diluted in 2.95 mL of PBS. The samples were applied directly to the fabricated sensors without any further treatment. As a reference measurement, the standard concentration of the virus (280 pg/mL) was included as a positive control, and untreated samples were taken as a negative control. The impedimetric signals of the tested sensors were investigated at DC 1.0 V in FCN/DCIP.

RT-PCR as a Confirmatory Assay. RT-PCR was conducted as a standard diagnostic method for the impedimetric tested clinical specimens. Briefly, the sample was exposed to viral RNA extraction using a QIAamp Viral-RNA kit (Qiagen, Germany). Then, the sample was tested for SARS-CoV-2 in a real-time RT-PCR using a Verso 1-step qRT-PCR kit (Thermo, USA) with the gene-specific primers and probes for the RT-PCR assay (Open Reading Frame 1ab (*ORF1ab*)-nsp14 gene assay).[21] A 25 μL total reaction mixture included a 5 μL template RNA, 1 μL of each forward and reverse primers (10 μM), 0.5 μL of the probe (10 μM), 1.25 μL of the RT-enhancer, 12.5 μL of 2× one-step buffer, 0.25 μL of an enzyme mixture, and 3.5 μL of ddH_2O. Thermal profile cycling was adjusted for reverse transcription and polymerase activation at 50 and 95 °C for 15 min/each. Subsequently, a denaturation process was subjected to 15 s at 95 °C for 45 cycles. Eventually, the annealing and extension processes were conducted at 60 °C for 30 s. The designed in-house synthetic plasmid was used as a positive control.

Statistics and Data Analysis. All data are presented as mean ± SD from at least three individual experiments. Statistical significance was determined by statistical hypothesis testing where the significance of the values was assumed to be $p < 0.05$. From the standard calibration curves, the limit of detection (LOD) and the limit of quantification (LOQ) were calculated. The reproducibility of the VIP sensor responses was represented by the relative standard deviation (RSD). Statistical analysis was performed using Origin-Lab software, which was used for drawing all presented figures.

RESULTS AND DISCUSSION

Electrode Surface Modification. To develop an effective impedimetric assay for the sensitive diagnosis of the coronavirus, electrode surfaces were modified with nanomaterials including carbon nanotubes (CNTs), fullerene, gold nanoparticles, manganese dioxide, and tungsten oxide (WO_3). The electrodes were characterized using cyclic voltammetry (CV) along with electrochemical impedance spectroscopy (EIS). The CNTs/WO_3-modified electrodes provided the highest electrochemical characteristics. Moreover, the EIS signals showed that the CNTs/WO_3 is providing the lowest charge transfer resistance (Figure 1A) due to the highest acquired electrocatalytic properties. Therefore, the CNTs/WO_3 nanocomposite is assigned as a base for the virus sensor construction.

SARS-CoV-2 Imprinting. Polymeric films of poly(meta-aminophenol) (Pm-AP) were in situ electrodeposited on the CNTs/WO_3 electrode in the presence of the whole SARS-CoV-2 particles to form a virus-imprinted matrix. To reach the best imprinting conditions, different voltammetric cycles, which varied from 15 to 60 cycles, were applied. For each formed imprinted layer, the sensing performance was evaluated using the target virus suspension. Accordingly, 30 cycles were chosen for the effective imprinting of the SARS-CoV-2 (Figure 1B).

SARS-CoV-2 Knock-Out from the VIP Matrix. The perfect removal of the whole virus particles from the imprinted matrix is necessary to create a complementary biorecognition element that will be applied for the specific detection. Therefore, several attempts were made, and according to the results presented in the Supporting Information, Figure S1, the best removal conditions were achieved when a mixture of acetic/citric acids was used. Both ethanol and sodium hypochlorite showed no significant changes in the EIS signals. Additionally, rinsing with 1% of Triton was performed to clean any remaining viral disrupted components. The efficacy of acids for the virus disruption is attributed to the lower pH as the proteins' protonation (i.e., protonation of the spike, envelope, and membrane proteins) causes conformational changes in the viral glycoproteins and induces viral envelope disintegration.[22] Otherwise, Triton dissociates the protein−lipid or the lipid−lipid interactions. Thus, acids and surfactants were selected for the complete virus disruption leaving the artificial complementary holes on the prepared sensor. Moreover, the period of washing was tested over different time intervals from 10 to 60 min at room temperature (Figure 1C). From the impedimetric response of each washing time, 30 min was assigned. As a control, all the previous washing attempts were applied to the non-imprinted virus (NIP surfaces) to assure that the washing protocol has no effect

https://doi.org/10.1021/acssensors.1c01614
ACS Sens. XXXX, XXX, XXX−XXX

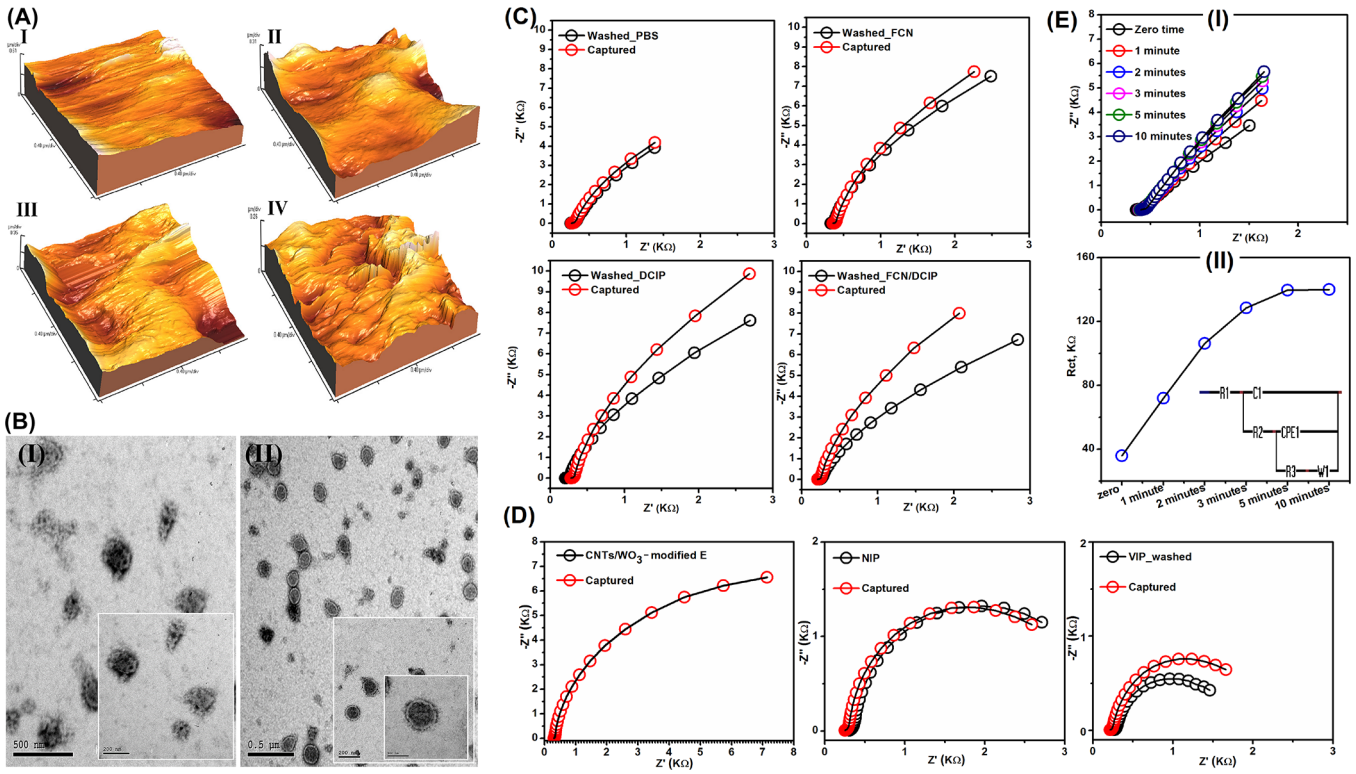

Figure 2. (A) AFM demonstrating the changes in the sensor morphology including nanomaterial modification (I), NIP (II), VIP (III), and the washed VIP (IV). The obtained surface roughnesses of the electrodes are 62, 55, 106, and 52 nm for the bare modified, NIP, VIP, and washed electrodes, respectively. (B) HR-TEM of the virucidal effect of the washing solutions on the virus shape and structure (I) versus the live virion with the intact and remarkable structure shape (II). (C) Testing the performance of the VIP sensor using single-mediated systems using FCN (0.3 mM), DCIP (100 μM), or double-mediated systems using a combination of FCN/DCIP. The resulting EIS signals were magnified in a double-mediating system. (D) Virus sensing performances of the nanomaterial-based surfaces, the NIP (only the polymeric matrix), and the VIP (the virus-imprinted surface). The EIS experiments were conducted in an FCN/DCIP mediator. (E) Binding time effects on the changes of the EIS signals. At a single-virus concentration, the VIP response was measured at different binding times (I). The time correlogram indicates that the R_{ct} increase was stable after 3 min (II). EIS data of the equivalent circuit model provided quantitative information on the actual changes in the charge transfer resistances (ΔR_{ct}). These data are shown in Table S2 (Supporting Information section).

on the formed polymeric matrix itself and the only effect is the virus structure damaging and digging it out from the VIP matrix. EIS data of the equivalent circuit model provided quantitative information on the actual changes in the charge transfer resistances. These data are shown in Table S1 (Supporting Information section).

Physicochemical Characterization of the Sensor's Surface. Topographical changes of the sensor surface were characterized using atomic force microscopy (AFM). A nanomaterial-coated surface was investigated where its average surface roughness was around 62 nm (Figure 2A-I). A distinct surface roughness (55 and 106 nm) existed between the non-imprinted virus (NIP) and the virus imprinted (VIP before knocking out the virus) (Figure 2A-II and III). This distinction is made due to the allocation of the complete virus particles within the poly(meta-aminophenol) matrix. Eventually, the washed VIP surfaces showed a surface roughness very similar to the NIP structure (~54 nm) (Figure 2A-IV). Further, microscopic analysis was conducted using transmission electron microscopy where the virucidal effect of the washing solution on the structural changes of the viral envelope was imaged. As a reference, a TEM image for the intact live virion was taken to show the characteristic structure and size of the whole virus particle (Figure 2B). Moreover, FE-SEM images were captured further to clarify the differences on the electrode surface (Supporting Information, Figure S2A). The distribution of $CNTs/WO_3$ onto the sensor surface was detected where the CNTs were aligned around the WO_3, which has an average particle size of 55 nm. The pure polymeric film of PmAP was layered regularly and covered the whole sensor surface. Unlike in the presence of SARS-CoV-2 particles, which were localized in the VIP matrix (Figure S2A-III), the created complementary binding sites were depicted (Figure S1B-IV).

The Fourier transform infrared (FTIR) spectra of the sensor components were investigated (Supporting Information, Figure S2B). Broad peaks were noticed at 3422 and 3300 cm^{-1} that correspond to the stretching vibrations of $-NH_2$ representing the PmAP formation and N−H in phenyl rings, respectively. A small peak at 2918 cm^{-1} was ascribed to the stretching vibration of C−H in the aromatic rings. Another sharp peak appeared at 1600 cm^{-1}, which is assigned to the C═C stretching vibrations of the benzene ring. As the electrochemical polymerization process of PmAP was carried out, a broad peak at 1200 cm^{-1} appeared, which is attributed to the C−O−C stretching vibrations.[23] Eventually, the presence of $-NH_2$ and C−O−C was designated to the formation of PmAP, and the intensity of the spectrum was lower in the case of the VIP, while the NIP and washed VIP were very similar.

Optimization of Sensing Parameters. In terms of monitoring the charge transfer resistance, testing the VIP sensor performance was evaluated either directly or using

https://doi.org/10.1021/acssensors.1c01614
ACS Sens. XXXX, XXX, XXX−XXX

artificial redox mediators such as FCN and DCIP (hydrophilic and lipophilic electron shuttles). Without the mediator, the impedance response was very weak as there was no remarkable EIS difference between the washed and captured surfaces. When the double-mediated system was applied, the EIS signals were significantly magnified (Figure 2C). As the sensor performance is derived by the selective localization of the virus particles into the created binding holes, a suspension of the target virus was introduced to the nanomaterial-coated surface, the NIP, and the VIP. From the EIS responses, the only electrochemical signal, as a response to the successful binding, was received from the VIP, which has the complementary binding sites (Figure 2D). Further, the binding time was tested from 5 to 10 min. Rapid binding has occurred as steady-state capturing reactions were achieved after 3 min (Figure 2E).

Calibration Curve. Under optimal conditions, the VIP sensor was in contact with different virus concentrations ranging from 7 to 320 pg/mL. For each measurement that represents each addition, the EIS responses were measured before and after the virus binding, where the change in the charge transfer resistance (ΔR_{ct}) was considered for drawing the calibration curve (Figure 3). The measurements were

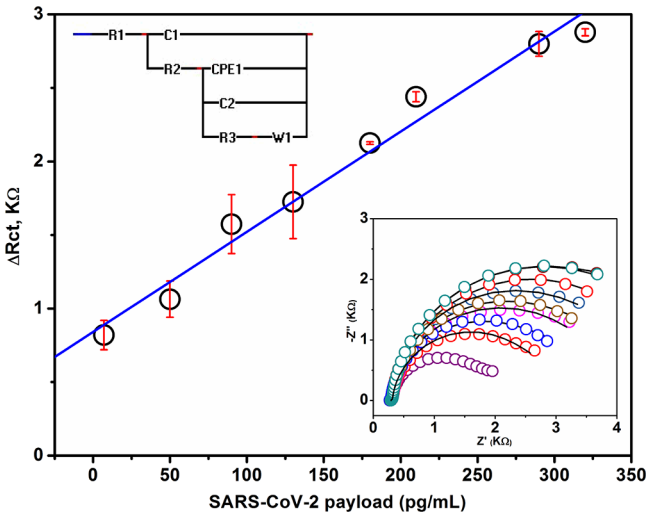

Figure 3. Calibration curve of different concentrations of SARS-CoV-2 particles ranging from 7 to 320 pg/mL. In a double-mediating electron shuttle, impedimetric responses were recorded for three successive readings. The ΔR_{ct} ($R_{ct\ captured} - R_{ct\ washed}$) was estimated by the designed Randles cell circuit from the fitted EIS signals. The correlation coefficient (R^2) was 0.989, and the P-value was <0.0001. The estimated LOD and LQD were 57 and 157 pg/mL, respectively. R1: solution resistance, C1: capacitance of the electrode surface, R2: resistance of the CNTs/WO_3 layer on the electrode surface, CPE1: constant phase elements of the inner layer of the electrode, C2: double-layer capacitance of polymerized meta-aminophenol (Pm-AP) on the sensor surface, R3: the resistance of the captured virus particles in the created pinholes on the VIP matrix, and W1: Warburg impedance for the diffusion of FCN/DCIP on the sensor interface.

tested at different direct potential ranges from 0.3 to 1 V where the remarkable impedimetric signals were achieved at 1 V (Supporting Information, Figure S3). From the calibration curve, the limits of detection (LOD) and quantification (LOQ) were 57 and 175 pg/mL, respectively. The correlation coefficient (R^2) was 0.989, and the P-value was <0.0001. The designed VIP sensor provides 27-fold more sensitivity than the adapted RT-PCR where the LOD was 3.7 copies/mL viral antigen for the proposed chips while about 100 copies/mL viral RNA for RT-PCR.[24] In another study, SARS-CoV-2 virus nucleic acid was extracted and detected by a MIP sensor based on SARS-CoV-2-N-protein. The estimated LOD of the study was 15 fM for the viral NA, which is more sensitive than our sensors.[19] However, our study does not rely on any sample preparation such as viral RNA extraction, which was necessary for the previous reports, but we deal directly with the virus load in the samples. Thus, the designed sensor offers the advantages of direct and quick detection of SARS-CoV-2 without any further treatment of the specimen.

Selectivity Test. Respiratory infections are caused by different circulating adapted interspecies transmitting respiratory viruses. The most commonly recognized types are the respiratory adenovirus, orthomyxoviruses, influenza A (H1N1, H3N2, and H5N1), Influenza B, human coronaviruses (hCoVs)-QC43, NL63, and 229E, and MERS-CoV. Accordingly, all these viruses were diagnosed using the designed VIP sensors to discriminate between the target virus from the other respiratory viruses. As a result, a very high selectivity with no obvious cross-reactivity was accomplished when the sensor was tested toward the H1N1, H5N1, and H3N2 influenza A-viruses (Figure 4). However, MERS-CoV and the other human coronaviruses triggered a positive-cross reactivity with about 2 and 36%, respectively.

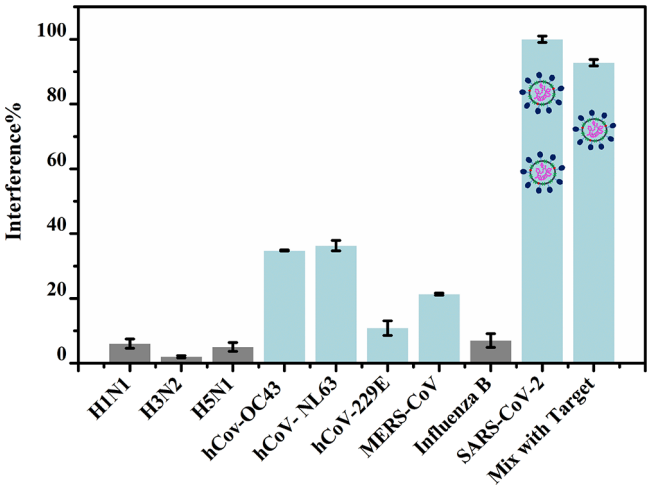

Figure 4. Selectivity test using respiratory interference viruses. The sensor showed no significant interference with the influenza viruses and a low interference response (20−36%) toward MERS-CoV and hCoVs.

Reproducibility, Accuracy, and Lifetime. Reproducibility of the sensor, which is very crucial, was monitored using three individual VIP chips, where the performance of each was evaluated using three different viral concentrations (100, 200, and 300 pg/mL). High reproducibility was obtained with a relative standard deviation of 3% (Supporting Information, Table S3). Furthermore, high repeatability was observed when the repeatability test was performed. On the other hand, the responses of the sensor chips were very stable over a long time without loss in the signal, especially in the first 2 months. Afterward, a 5% decrease in response was noticed. Ultimately, the sensor accuracy was validated using six spiked samples (S1, S2, S3, S4, S5, and S6) with different virus payloads (50, 130, 190, 260, 280, and 340 pg/mL, respectively) in three

https://doi.org/10.1021/acssensors.1c01614
ACS Sens. XXXX, XXX, XXX−XXX

replicates. The estimated accuracy was about 97% toward the spiked samples, as given in the Supporting Information, Table S4.

Clinical Application. In SARS-CoV-2 diagnosis, nasopharyngeal or oropharyngeal swabs are the most reliant sample sources. Therefore, 23 samples (labeled with S1 to S23) were collected from nasopharyngeal swabs and they were tested using the VIP sensor, as demonstrated in Figure 5. Out of the 23 specimens tested, 20 samples were SARS-CoV-2 positively confirmed and three were negative cases. Using the current sensor, quantitative analysis of the viral payload in each clinical specimen was determined, and all data are provided in Table 1 in comparison with the PCR results. To that end, the virus payloads of the S1 and S2 were 240 and 210 pg/mL, respectively, and these virus concentrations correspond to the impedimetric signals (1.80 ± 0.022 and 1.60 ± 0.064 KΩ, respectively). Samples (S3 to S13) were infected with viral payloads of 140, 133, 132, 129, 149, 124, 118, 120, 119, 120, and 113 pg/mL, respectively. Definitely, the proposed sensor has great potential for measuring the concentration of the virus antigen in the SARS-CoV-2-positive patients' samples. Additionally, the resulting ΔR_{ct} values for S14, S16, and S18 were 0.6 ± 0.059, 0.637 ± 0.070, and 0.535 ± 0.016 KΩ, respectively, and the evaluated virus concentrations were 80, 58, 72, and 90 pg/mL, respectively. The PCR report of those samples confirmed the positivity at Ct of 30, 31, and 35, respectively. Despite S15, S17, and S19 being SARS-CoV-2-positive by the PCR cutting the threshold line at cycles 31, 33, and 35, respectively, the impedimetric signals (0.809 ± 0.016, 0.828 ± 0.044, and 0.777 ± 0.029 KΩ) reflected the practical response of the proposed sensor toward the target virus and confirmed that the resulting Cts of PCR cannot provide viral payload in the tested sample.[25] The virus concentrations of S15, S17, and S19 were 108, 111, and 104 pg/mL, respectively. The positivity of PCR was detected at cut off for the Ct value ≤35, despite that S20 resulted in the SARS-CoV-2-negative

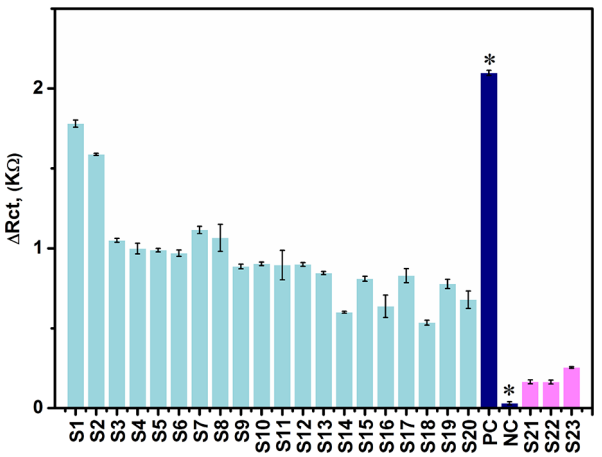

Figure 5. Application of the fabricated SARS-CoV-2 sensor on the clinical samples referring to the positive control, PC (target, 0.3 ng/mL), and the negative control, NC. S# stands for the number of collected clinical samples.

Table 1. Application of the SARS-CoV-2 VIP Sensor on the Clinical Specimens Compared with the rT-RT-PCR[a]

		rT-RT-PCR		nanostructured SARS-CoV-2 sensor	
sample no.	sample origin	cycle threshold (Ct)	copy number/reaction	ΔR_{ct} ($R_{ct\ captured} - R_{ct\ washed}$) KΩ ± SD	antigenic payload (pg/mL)
S1	nasopharyngeal swab	19.4	7.6	1.8 ± 0.022	240
S2		21	7.16	1.6 ± 0.064	210
S3		22	6.86	1.05 ± 0.012	140
S4		22	6.86	0.999 ± 0.033	133
S5		22.45	6.7	0.988 ± 0.011	132
S6		23	6.56	0.969 ± 0.019	129
S7		23	6.56	1.15 ± 0.023	149
S8		23.6	6.38	1.065 ± 0.084	142
S9		24	6.26	0.887 ± 0.014	118
S10		26	5.67	0.903 ± 0.011	120
S11		26.8	5.47	0.895 ± 0.092	119
S12		27	5.4	0.899 ± 0.012	120
S13		28	5.11	0.845 ± 0.010	113
S14		30.23	4.44	0.60 ± 0.059	80
S15		31	4.2	0.810 ± 0.016	108
S16		31	4.2	0.637 ± 0.070	85
S17		33	3.6	0.829 ± 0.044	111
S18		34.6	3.12	0.535 ± 0.016	72
S19		35	3	0.778 ± 0.029	104
S20		37	NA	0.678 ± 0.054	90
S21		>45	NA	0.165 ± 0.012	NA
S22		>45	NA	0.164 ± 0.012	NA
S23		>45	NA	0.254 ± 0.049	NA

[a]Specimens were tested using the VIP sensor, and the investigated impedimetric signals were analyzed, and according to the calibration standard curve provided, the viral payload in the specimen was estimated in pg/mL. The positive control (PC, 2.079 KΩ ± 0.016 (300 pg/mL)) and the negative control (NC, 0.030 ± 0.010 KΩ) were included in the test. The specimens were tested using rT-RT-PCR as a confirmative and a comparative step for the efficiency of the fabricated electrochemical sensor, and the results were obtained as cutting a threshold line at different cycles according to the genomic representation in the tested specimen. The copy number of the viral nucleic acid/reaction was estimated according to the standard calibration curve ($y = -3.3418x + 44.938$), where y is the investigated Ct and x is the copy number.

https://doi.org/10.1021/acssensors.1c01614
ACS Sens. XXXX, XXX, XXX−XXX

sample by PCR (cut off at 37), but after the application on the chip, the ΔR_{ct} was 0.678 ± 0.054 KΩ with 90 pg/mL. Moreover, three SARS-CoV-2-negative samples (Ct >45 using PCR) were tested (Table 1). Based on these validated results, the VIP sensor can rapidly quantify the SARS-CoV-2 concentration in the virus-infected cases and differentiate between the infected, contact, and healthy persons.

CONCLUSIONS

A nanostructured-based SARS-CoV-2-VIP sensor was fabricated for the rapid, selective, and accurate diagnosis of SARS-CoV-2 in clinical samples. As a sensor platform, CNTs/WO_3 was implemented to enhance the surface performance and whole virus imprinting. The composite showed its electrochemical and electron transfer efficacy over the other nanoparticles. For the highly competent VIP sensor, the electrochemical polymerization method was optimized including the 30 voltammetric cycles for the perfect coating of the Pm-AP on the modified electrode besides the washing step (citric/acetic/Triton) for virus removal to create the complementary binding sites for SARS-CoV-2 pick up. Furthermore, the EIS parameters were optimized for the effective impedimetric signals as the effective DC potential was at 1.0 V for the double-mediating FCN/DCIP system, which resulted in signal magnification. Thus, the whole virus particles were electrochemically imprinted into a polymeric matrix and a double-mediated electron system was used for monitoring the binding responses in terms of selectivity and sensitivity. Indeed, the sensor provided a rapid and sensitive detection platform with a detection limit of 57 pg/mL (3.7 copy/mL), 27-fold more sensitive than RT-PCR. A wide range of interferent viruses were used for testing the competence of the designed sensors to discriminate between the target virus from the other interference respiratory viruses. Hence, the sensor was successfully applied in the diagnosis of clinical specimens while the rT-RT-PCR was considered as the reference method. Regarding the global panic state caused by SARS-CoV-2, the suspected patients could be diagnosed quickly within 5 min and accurately using the provided sensor by the direct application of a nasopharyngeal swab on the VIP chip with no need of a well-equipped laboratory. Quantitative measurements could be investigated after the chip integration with a portable electrochemical device. Therefore, the sensor can be used in hospitals, airports, schools, and hotspot regions. As a promising point-of-care (POC) device for the rapid and selective SARS-CoV-2 diagnosis, this VIP sensor is highly recommended.

ASSOCIATED CONTENT

Supporting Information

The Supporting Information is available free of charge at https://pubs.acs.org/doi/10.1021/acssensors.1c01614.

Virus-imprinted chips for early and rapid diagnosis, washing step study using different washing solutions (ethanol, hypochlorite, and citric/acetic acids) with a significant response observed in the case of citric/acetic-treated electrodes (Figure S1), morphological characterization of the imprinted sensors using SEM and FTIR (Figure S2), and capturing capacity study using different spiked virus concentrations and electrodes that were investigated at wide ranges of DC (0.3−1 V) with the effective investigating potential carried out at a 1 V direct current (Figure S3) (PDF)

(PDF)

AUTHOR INFORMATION

Corresponding Author

Rabeay Y. A. Hassan − *Nanoscience Program, University of Science and Technology (UST), Zewail City of Science and Technology, Giza 12578, Egypt; Applied Organic Chemistry Department, National Research Centre (NRC), 12622 Giza, Egypt;* orcid.org/0000-0002-1867-9643; Email: ryounes@zewailcity.edu.eg

Authors

Heba A. Hussein − *Virology Department, Animal Health Research Institute (AHRI), Agricultural Research Center (ARC), Giza 12619, Egypt;* orcid.org/0000-0003-1058-4946

Ahmed Kandeil − *Center of Scientific Excellence for Influenza Viruses, Environmental Research Division, National Research Centre, Giza 12622, Egypt*

Mokhtar Gomaa − *Center of Scientific Excellence for Influenza Viruses, Environmental Research Division, National Research Centre, Giza 12622, Egypt*

Rasha Mohamed El Nashar − *Chemistry Department, Faculty of Science, Cairo University, Giza 12613, Egypt;* orcid.org/0000-0001-6150-8420

Ibrahim M. El-Sherbiny − *Nanoscience Program, University of Science and Technology (UST), Zewail City of Science and Technology, Giza 12578, Egypt;* orcid.org/0000-0002-8179-437X

Complete contact information is available at: https://pubs.acs.org/10.1021/acssensors.1c01614

Author Contributions

H.A.H. performed the electrochemical experiments and wrote the original draft of the manuscript. A.K. conducted the virology experiments. M.G. contributed to clinical sample preparation and validation using the PCR. R.M.E.N. reviewed the manuscript. I.M.E.-S. reviewed the manuscript. R.Y.A.H. devised the project, designed the conceptual idea and proof outline, analyzed the results, and revised the manuscript. All authors gave approval to the current version of the manuscript.

Notes

The authors declare no competing financial interest.

According to the community-based cohort study of SARS-CoV-2 in Egypt, the in vitro clinical study is accomplished in agreement with the appropriate ethical guidelines. The approval for the study was granted by the IRBs of St. Jude Children's Research Hospital (USA) (reference number 007079) and the Research Ethics Committee of the National Research Centre (NCR, Egypt) (protocol number 14155).

ACKNOWLEDGMENTS

This project is fully funded by the ASRT-Cairo Egypt. Therefore, we acknowledge the Egyptian Academy of Scientific Research and Technology (ASRT, Cairo, Egypt) for funding the research project entitled SARS-COV2-Biosensor: Disposable chips for the early and rapid diagnosis (project ID: ASRT 7314-COVID Emergency call through the Ideation Fund program). Special thanks to Prof. Dr. Mohamed Ahmed Ali

(National Research Centre, NRC, Cairo, Egypt) for offering his virological materials and lab facilities.

REFERENCES

(1) Gorbalenya, A. E.; Baker, S. C.; Baric, R. S.; de Groot, R. J.; Drosten, C.; Gulyaeva, A. A.; Haagmans, B. L.; Lauber, C.; Leontovich, A. M.; Neuman, B. W.; Penzar, D. Coronaviridae Study Group of the International Committee on Taxonomy of Viruses. The species Severe acute respiratory syndrome-related coronavirus: classifying 2019-nCoV and naming it SARS-CoV-2. *Nat. Microbiol.* **2020**, *5*, 536−544.

(2) Hussein, H. A.; Hassan, R. Y. A.; Chino, M.; Febbraio, F. Point-of-Care Diagnostics of COVID-19: From Current Work to Future Perspectives. *Sensors* **2020**, *20*, 4289.

(3) Yelagandula, R.; Bykov, A.; Vogt, A.; Heinen, R.; Özkan, E.; Strobl, M. M.; Baar, J. C.; Uzunova, K.; Hajdusits, B.; Kordic, D.; Suljic, E.; Kurtovic-Kozaric, A.; Izetbegovic, S.; Schaeffer, J.; Hufnagl, P.; Zoufaly, A.; Seitz, T.; Al-Rawi, M.; Ameres, S.; Baar, J.; Bauer, B.; Beer, N.; Bergauer, K.; Binder, W.; Blaukopf, C.; Bochev, B.; Brennecke, J.; Brinnich, S.; Bundalo, A.; Busslinger, M.; Clausen, T.; de Vries, G.; Dekens, M.; Drechsel, D.; Dzupinkova, Z.; Eckmann-Mader, M.; Fellner, M.; Fellner, T.; Fin, L.; Gapp, B. V.; Grabmann, G.; Grishkovskaya, I.; Hagelkruys, A.; Handler, D.; Haselbach, D.; Hempel, L.; Hill, L.; Hoffmann, D.; Horer, S.; Isemann, H.; Kalis, R.; Kellner, M.; Kley, J.; Köcher, T.; Köhler, A.; Krauditsch, C.; Kula, S.; Lang, S.; Latham, R.; Leitner, M.-C.; Leonard, T.; Lindenhofer, D.; Manzenreither, R. A.; Matl, M.; Mechtler, K.; Meinhart, A.; Mereiter, S.; Micheler, T.; Moeseneder, P.; Neumann, T.; Nimpf, S.; Nordborg, M.; Ogris, E.; Pagani, M.; Pauli, A.; Peters, J.-M.; Pjevac, P.; Plaschka, C.; Rath, M.; Reumann, D.; Rieser, S.; Rocha-Hasler, M.; Rodriguez, A.; Ropek, N.; Ross, J. J.; Scheuch, H.; Schindler, K.; Schmidt, C.; Schmidt, H.; Schnabl, J.; Schüchner, S.; Schwickert, T.; Sommer, A.; Soldoroni, D.; Stadlmann, J.; Steinlein, P.; Strobl, M.; Strobl, S.; Sun, Q.; Tang, W.; Trübestein, L.; Trupke, J.; Umkehrer, C.; Urmosi-Incze, S.; Versteeg, G.; Vogt, V.; Wagner, M.; Weissenboeck, M.; Werner, B.; Zuber, J.; Födinger, M.; Allerberger, F.; Stark, A.; Cochella, L.; Elling, U. Multiplexed detection of SARS-CoV-2 and other respiratory infections in high throughput by SARSeq. *Nat. Commun.* **2021**, *12*, 3132.

(4) Huang, C.; Wang, Y.; Li, X.; Ren, L.; Zhao, J.; Hu, Y.; Zhang, L.; Fan, G.; Xu, J.; Gu, X.; Cheng, Z.; Yu, T.; Xia, J.; Wei, Y.; Wu, W.; Xie, X.; Yin, W.; Li, H.; Liu, M.; Xiao, Y.; Gao, H.; Guo, L.; Xie, J.; Wang, G.; Jiang, R.; Gao, Z.; Jin, Q.; Wang, J.; Cao, B. Clinical features of patients infected with 2019 novel coronavirus in Wuhan, China. *Lancet* **2020**, *395*, 497−506.

(5) Chan, J. F.-W.; Yuan, S.; Kok, K.-H.; To, K. K.-W.; Chu, H.; Yang, J.; Xing, F.; Liu, J.; Yip, C. C.-Y.; Poon, R. W.-S.; Tsoi, H.-W.; Lo, S. K.-F.; Chan, K.-H.; Poon, V. K.-M.; Chan, W.-M.; Ip, J. D.; Cai, J.-P.; Cheng, V. C.-C.; Chen, H.; Hui, C. K.-M.; Yuen, K.-Y. A familial cluster of pneumonia associated with the 2019 novel coronavirus indicating person-to-person transmission: a study of a family cluster. *Lancet* **2020**, *395*, 514−523.

(6) Letko, M.; Marzi, A.; Munster, V. Functional assessment of cell entry and receptor usage for SARS-CoV-2 and other lineage B betacoronaviruses. *Nat. Microbiol.* **2020**, *5*, 562−569.

(7) Hoffmann, M.; Kleine-Weber, H.; Schroeder, S.; Krüger, N.; Herrler, T.; Erichsen, S.; Schiergens, T. S.; Herrler, G.; Wu, N. H.; Nitsche, A.; Müller, M. A.; Drosten, C.; Pöhlmann, S. SARS-CoV-2 Cell Entry Depends on ACE2 and TMPRSS2 and Is Blocked by a Clinically Proven Protease Inhibitor. *Cell* **2020**, *181*, 271−280.e8.

(8) Liu, Z.; Xiao, X.; Wei, X.; Li, J.; Yang, J.; Tan, H.; Zhu, J.; Zhang, Q.; Wu, J.; Liu, L. Composition and divergence of coronavirus spike proteins and host ACE2 receptors predict potential intermediate hosts of SARS-CoV-2. *J. Med. Virol.* **2020**, *92*, 595−601.

(9) Chan, J. F.-W.; Kok, K.-H.; Zhu, Z.; Chu, H.; To, K. K.-W.; Yuan, S.; Yuen, K. Y. Genomic characterization of the 2019 novel human-pathogenic coronavirus isolated from a patient with atypical pneumonia after visiting Wuhan. *Emerging Microbes Infect.* **2020**, *9*, 221−236.

(10) Long, Q.-X.; Liu, B.-Z.; Deng, H.-J.; Wu, G.-C.; Deng, K.; Chen, Y.-K.; Liao, P.; Qiu, J.-F.; Lin, Y.; Cai, X.-F.; Wang, D.-Q.; Hu, Y.; Ren, J.-H.; Tang, N.; Xu, Y.-Y.; Yu, L.-H.; Mo, Z.; Gong, F.; Zhang, X.-L.; Tian, W.-G.; Hu, L.; Zhang, X.-X.; Xiang, J.-L.; Du, H.-X.; Liu, H.-W.; Lang, C.-H.; Luo, X.-H.; Wu, S.-B.; Cui, X.-P.; Zhou, Z.; Zhu, M.-M.; Wang, J.; Xue, C.-J.; Li, X.-F.; Wang, L.; Li, Z.-J.; Wang, K.; Niu, C.-C.; Yang, Q.-J.; Tang, X.-J.; Zhang, Y.; Liu, X.-M.; Li, J.-J.; Zhang, D.-C.; Zhang, F.; Liu, P.; Yuan, J.; Li, Q.; Hu, J.-L.; Chen, J.; Huang, A.-L. Antibody responses to SARS-CoV-2 in patients with COVID-19. *Nat. Med.* **2020**, *26*, 845−848.

(11) Hussein, H. A.; Hassan, R. Y. A.; El Nashar, R. M.; Khalil, S. A.; Salem, S. A.; El-Sherbiny, I. M. Designing and fabrication of new VIP biosensor for the rapid and selective detection of foot-and-mouth disease virus (FMDV). *Biosens. Bioelectron.* **2019**, *141*, 111467.

(12) Anusha, T.; Sai Bhavani, K.; Shankumkha Kumar, J. V.; Kumar Brahman, P.; Hassan, R. Y. A. Fabrication of electrochemical immunosensor based on GCN-β-CD/Au nanocomposite for the monitoring of vitamin D deficiency. *Bioelectrochemistry* **2022**, 107935.

(13) Iravani, S. Nano- and biosensors for the detection of SARS-CoV-2: challenges and opportunities. *Mater. Adv.* **2020**, *1*, 3092−3103.

(14) Seo, G.; Lee, G.; Kim, M. J.; Baek, S.-H.; Choi, M.; Ku, K. B.; Lee, C.-S.; Jun, S.; Park, D.; Kim, H. G.; Kim, S.-J.; Lee, J.-O.; Kim, B. T.; Park, E. C.; Kim, S. I. Rapid Detection of COVID-19 Causative Virus (SARS-CoV-2) in Human Nasopharyngeal Swab Specimens Using Field-Effect Transistor-Based Biosensor. *ACS Nano* **2020**, *14*, 5135−5142.

(15) Moitra, P.; Alafeef, M.; Dighe, K.; Frieman, M. B.; Pan, D. Selective Naked-Eye Detection of SARS-CoV-2 Mediated by N Gene Targeted Antisense Oligonucleotide Capped Plasmonic Nanoparticles. *ACS Nano* **2020**, *14*, 7617−7627.

(16) Alafeef, M.; Dighe, K.; Moitra, P.; Pan, D. Rapid, Ultrasensitive, and Quantitative Detection of SARS-CoV-2 Using Antisense Oligonucleotides Directed Electrochemical Biosensor Chip. *ACS Nano* **2020**, *14*, 17028−17045.

(17) Cui, F.; Zhou, Z.; Zhou, H. S. Molecularly Imprinted Polymers and Surface Imprinted Polymers Based Electrochemical Biosensor for Infectious Diseases. *Sensors* **2020**, *20*, 996.

(18) Hussein, H. A.; El Nashar, R. M.; El-Sherbiny, I. M.; Hassan, R. Y. A. High selectivity detection of FMDV- SAT-2 using a newly-developed electrochemical nanosensors. *Biosens. Bioelectron.* **2021**, *191*, 113435.

(19) Raziq, A.; Kidakova, A.; Boroznjak, R.; Reut, J.; Öpik, A.; Syritski, V. Development of a portable MIP-based electrochemical sensor for detection of SARS-CoV-2 antigen. *Biosens. Bioelectron.* **2021**, *178*, 113029.

(20) Kandeil, A.; Mostafa, A.; El-Shesheny, R.; Shehata, M.; Roshdy, W. H.; Ahmed, S. S.; Gomaa, M.; Taweel, A. E.; Kayed, A. E.; Mahmoud, S. H.; Moatasim, Y.; Kutkat, O.; Kamel, M. N.; Mahrous, N.; Sayes, M. E.; Guindy, N. M. E.; Naguib, A.; Ali, M. A. Coding-Complete Genome Sequences of Two SARS-CoV-2 Isolates from Egypt. *Microbiol. Resour. Announce.* **2020**, *9*, No. e00489-20.

(21) Chu, D. K. W.; Pan, Y.; Cheng, S. M. S.; Hui, K. P. Y.; Krishnan, P.; Liu, Y.; Ng, D. Y. M.; Wan, C. K. C.; Yang, P.; Wang, Q.; Peiris, M.; Poon, L. L. M. Molecular Diagnosis of a Novel Coronavirus (2019-nCoV) Causing an Outbreak of Pneumonia. *Clin. Chem.* **2020**, *66*, 549−555.

(22) Pianta, L.; Vinciguerra, A.; Bertazzoni, G.; Morello, R.; Mangiatordi, F.; Lund, V. J.; Trimarchi, M. Acetic acid disinfection as a potential adjunctive therapy for non-severe COVID-19. *Eur. Arch. Otorhinolaryngol.* **2020**, *277*, 2921−2924.

(23) Kong, Y.; Zhou, Y.; Shan, X.; Jiang, Y.; Yao, C. Electropolymerization of m-aminophenol on expanded graphite and its electrochemical properties. *Synth. Met.* **2011**, *161*, 2301−2305.

(24) Arnaout, R.; Lee, R. A.; Lee, G. R.; Callahan, C.; Yen, C. F.; Smith, K. P.; Arora, R.; Kirby, J. E. SARS-CoV2 Testing: The Limit of Detection Matters. *bioRxiv* **2020**, DOI: 10.1101/2020.06.02.131144.

https://doi.org/10.1021/acssensors.1c01614
ACS Sens. XXXX, XXX, XXX−XXX

(25) Han, M. S.; Byun, J. H.; Cho, Y.; Rim, J. H. RT-PCR for SARS-CoV-2: quantitative versus qualitative. *Lancet Infect. Dis.* **2021**, *21*, 165.

https://doi.org/10.1021/acssensors.1c01614
ACS Sens. XXXX, XXX, XXX−XXX